Science Advances
AAAS

Supplementary Materials for

Spiral self-assembly of lamellar micelles into multi-shelled hollow nanospheres with unique chiral architecture

Liang Peng, Huarong Peng, Yu Liu, Xiao Wang, Chin-Te Hung, Zaiwang Zhao, Gang Chen, Wei Li*, Liqiang Mai, Dongyuan Zhao*

*Corresponding author. Email: weilichem@fudan.edu.cn (W.L.); dyzhao@fudan.edu.cn (D.Z.)

Published 3 November 2021, *Sci. Adv.* **7**, eabi7403 (2021)
DOI: 10.1126/sciadv.abi7403

The PDF file includes:

Other Supplementary Material for this manuscript includes the following:

Materials and Methods

Chemicals. Dopamine hydrochloride ($C_8H_{11}NO_2$•HCl, DA), Pluronic P105 ($PEO_{37}PPO_{56}PEO_{37}$), Pluronic F108 ($PEO_{132}PPO_{50}PEO_{132}$), Pluronic P123 ($PEO_{20}PPO_{70}PEO_{20}$) and Pluronic F127 ($PEO_{106}PPO_{70}PEO_{106}$) were purchased from Sigma-Aldrich. 1, 3, 5-trimethylbenzene (C_9H_{12}, TMB), ammonium hydroxide (NH_3 •H_2O, 28-30 wt%) and ethanol (C_2H_6O) were purchased from Shanghai Chemical Corp. All the reagents were directly used without further purification.

Synthesis of the spiral multi-shelled polydopamine (PDA) and carbon nanospheres with unique chiral architecture. In a typical synthesis, 1.0 g of Pluronic P123, 0.75 g of DA and 1.0 mL of TMB were successively dissolved in a mixture consist of 50 mL of ethanol and 50 mL of water by stirring at 300 rpm for 15 min to form a lamellar micelles system. Then, 1.5 mL of NH_3 • H_2O was added to induce the polymerization of DA precursor. The intermediate products of as-made mesostructured PDA nanospheres were collected by centrifugation after 3.0 h and then washed with ethanol and water several times. The experiment was carried out at a temperature of 25 ℃. To obtain the spiral multi-shelled carbon nanospheres (MCNs), the freeze-dried as-made mesostructured PDA nanospheres were heated at 350 °C for 3.0 h and subsequently heated at 900 °C for 2.0 h under N_2 atmosphere with a heating rate of 1.0 °C min^{-1}.

Control experiments in the micelles-directed self-assembly strategy.

Change in the template. The synthetic processes were carried out similarly as described above except that the templates were adjusted to Pluronic F127, Pluronic P105 and Pluronic F108, respectively. The formed polymer products were collected and calcined

at 350 °C for 3.0 h and subsequently at 900 °C for 2.0 h with a heating rate of 1.0 °C min^{-1}.

Change in the volume fraction of ethanol to water. The synthetic processes were conducted similarly except that the volume fraction of ethanol to water was changed from 20 %, 80 %, and 100 %. The resultant polymer products were collected and calcined at 350 °C for 3.0 h and subsequently at 900 °C for 2.0 h with a heating rate of 1.0 °C min^{-1}.

Change in the TMB/P123 mass ratio. The synthetic processes were performed similarly except that the TMB/P123 mass ratios were changed from 0.2, to 0.4, and to 1.2. The polymer products were collected and calcined at 350 °C for 3.0 h and subsequently at 900 °C for 2.0 h with a heating rate of 1.0 °C min^{-1}.

Change in the dopamine amount. The synthetic processes were performed similarly except that the dopamine amounts were changed from 0.25, to 0.50, and to 1.5 g. The polymer products were collected and calcined at 350 °C for 3.0 h and subsequently at 900 °C for 2.0 h with a heating rate of 1.0 °C min^{-1}.

Change in the stirring rate. The synthetic processes were carried out on similarly except for adjusting the stirring rate from 0, 700, and 1000 rpm. The polymer products were collected and calcined at 350 °C for 3.0 h and subsequently at 900 °C for 2.0 h with a heating rate of 1.0 °C min^{-1}.

Materials characterization.

Field-emission scanning electron microscopy (FESEM) images were conducted on a Hitachi Model S-4800 microscopy (Japan) with a landing energy of 5 kV.

Transmission electron microscopy (TEM) was performed on a JEOL JEM-2011F microscope (Japan) with an operation voltage of 200 kV, which is equipped with STEM and EDS detectors for elemental mapping analysis. TEM tomography was performed on a FEI Tecnai G2 electron microscope operated at 200 kV. Samples used for TEM and FESEM analyses were prepared by dropping of the polymers/carbons in ethanol on amorphous carbon-coated copper grids and silicon substrates, respectively. Wide angle powder X-ray diffraction (XRD) patterns were recorded on a Bruker D4 X-ray diffractometer (Germany) with Ni-filtered Cu Kα radiation (40 kV, 40 mA). The N_2 sorption isotherms were measured on a Micromeritcs Tristar 2420 analyzer (USA) at 77 K. Before measurements, all of the samples were degassed at 180 °C under vacuum for at least 8 h. The Brunauer-Emmett-Teller (BET) method was used to calculate the specific surface areas (S_{BET}) using the adsorption data in the relative pressure (P/P_0) range from 0.005 to 0.25. The pore size distributions and the total pore volumes (V_t) were derived from the adsorption branches of isotherms and the relative pressure (P/P_0) at 0.995, respectively, using the Barrett-Joyner-Halenda (BJH) model. Synchrotron radiation small-angle X-ray scattering (SAXS) measurements were conducted at Beamline 16B (SSRF, China). The *d*-spacing values were calculated using the formula $d = 2\pi/q$, where q is wave-vector transfer, given by $q = 4\pi (\sin\theta)/\lambda$. X-ray photoelectron spectroscopy (XPS) was recorded on an AXIS ULTRA DLD XPS system (Shimadzu Corp) with MONO Al source. All of the binding energies were referenced to the C 1s standard peak at 284.6 eV. Raman spectra were recorded using a Dilor LabRam-1B microscopic Raman spectrometer (France), using a He-Ne laser

with an excitation wavelength of 632.8 nm. Thermogravimetric analysis (TGA) was conducted using a Mettler Toledo TGA/SDTA851 analyzer (Switzerland) under N_2 atmosphere from 50 to 900 °C with a heating rate of 5 °C min^{-1}. Fourier-transform infrared (FTIR) spectra were recorded on a PerkinElmer Spectrum II FTIR Spectrometer. Circular dichroism (CD) spectra were measured on a BioLogic MOS-450 spectropolarimeter. Ultraviolet-visible (UV-Vis) diffuse reflectance spectrum was collected on Lambda 650S UV spectrophotometer. Solid state nuclear magnetic resonance (NMR) spectrum was selected on a Bruker AVANCE III 400 WB spectrometer.

Electrochemical Measurements.

All the electrochemical measurements were conducted using the CR2032 coin type half-cells. The working electrode was made in a homogeneous slurry containing 10 wt % of polyvinylidene fluoride (PVDF), 10 wt% acetylene black and 80 wt % of the active material in N-methyl-pyrrolidone. The slurry was thoroughly mixed and casted on Cu foil and then dried in vacuum overnight. A potassium foil was used as the counter electrode, and Whatman glass fiber was used as the separator. The electrolyte used was a mixture of 0.8 M KPF_6 in diethyl carbonate (DEC) and ethylene carbonate (EC) with a volume ratio of 1:1. For lithium ion battery, the lithium foil and a solution of 1.0 M $LiPF_6$ in DEC, EC and ethyl methyl carbonate (EMC) with a volume ratio of 1:1:1 were used as counter electrode and electrolyte, respectively. The coin cells were assembled in an argon-filled glovebox. The Galvanostatic cycling and rate performance were conducted using a LAND-CT2001A battery-testing system at room temperature in the

voltage range of 0.01-3.0 V. Cyclic voltammetry (CV) was performed on a CHI 660E workstation (CH Instruments) from 0.1 to 2.0 mV s^{-1} between 0.01 and 3.0 V. The specific capacity was normalized to the mass of the active materials.

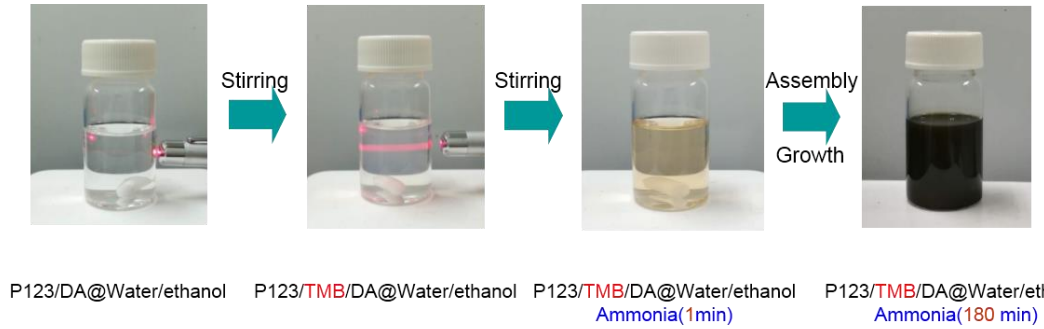

Fig. S1. Photos of the color transformations of the reaction system during the self-assembly process. It can be seen that the reactant solution undergoes a series transform from a clear transparent solution to a light white emulsion, then to a brown suspension, and finally to a deep black mixture. (Photo Credit: L. Peng, Fudan University)

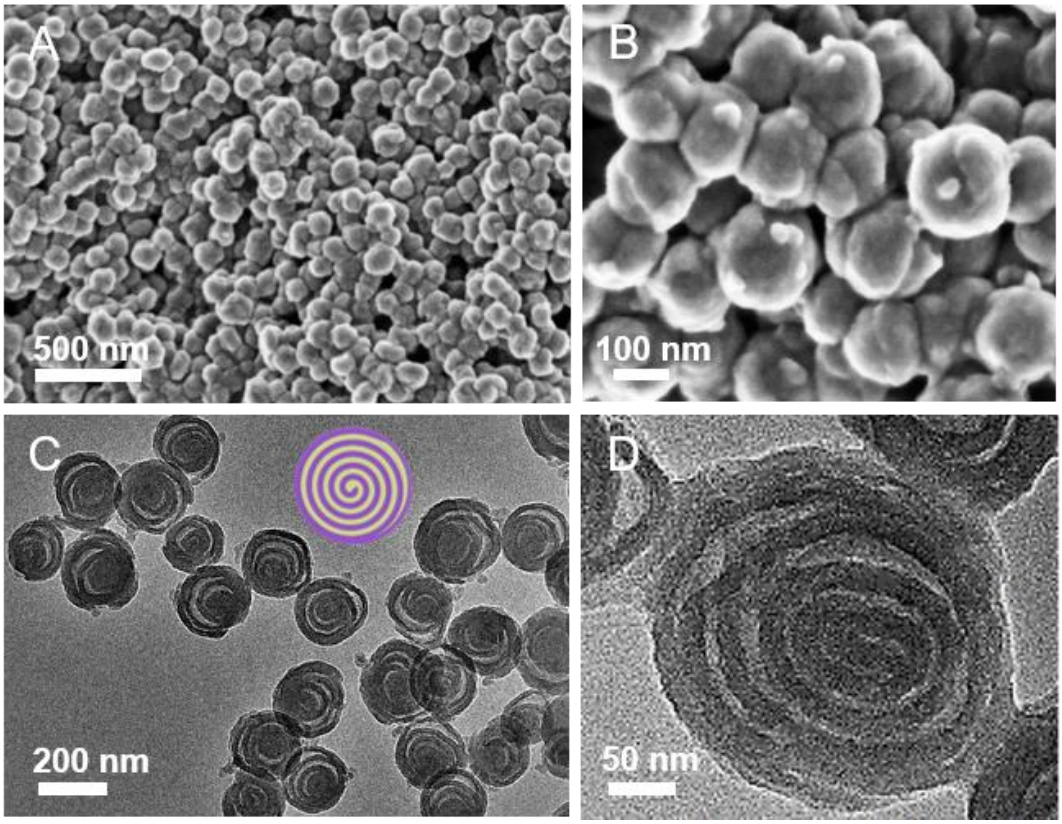

Fig. S2. Structural characterizations of the as-made PDA nanospheres. (A, B) FESEM and (C, D) TEM images of the as-made PDA nanospheres prepared by the lamellar micelle spiral self-assembly strategy. The as-made PDA nanospheres were prepared by using Pluronic P123 as the soft template, TMB as the hydrophobic interaction mediation agent, and DA as the nitrogen and carbon source in an ethanol/water mixture. It can be seen that the as-made PDA nanospheres are very uniform with a small particle size of ~180 nm and possess a spiral multi-shelled hollow nanostructure with an average interlayer spacing of ~20 nm.

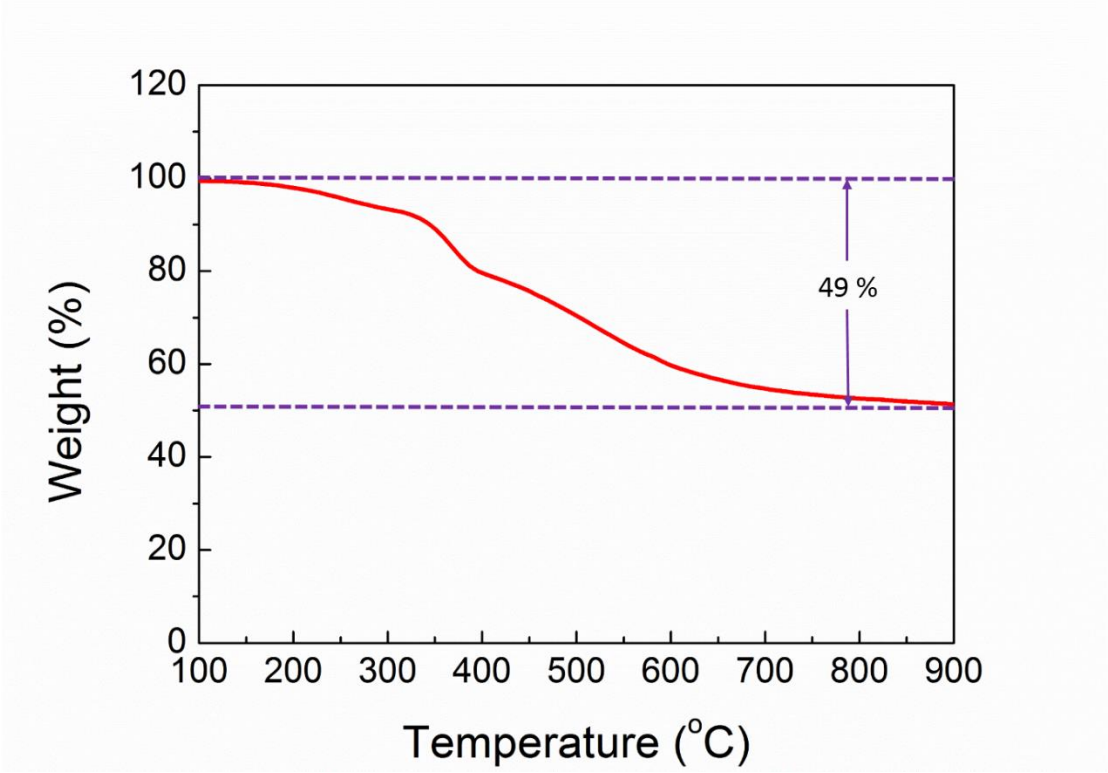

Fig. S3. TGA curve of the as-made PDA nanospheres. The TGA curve of the as-made PDA nanospheres prepared by the lamellar micelle spiral self-assembly strategy. The result indicates that the carbonization process starts at around 350 °C and the carbon yield is as high as ~51 wt% at 900 °C.

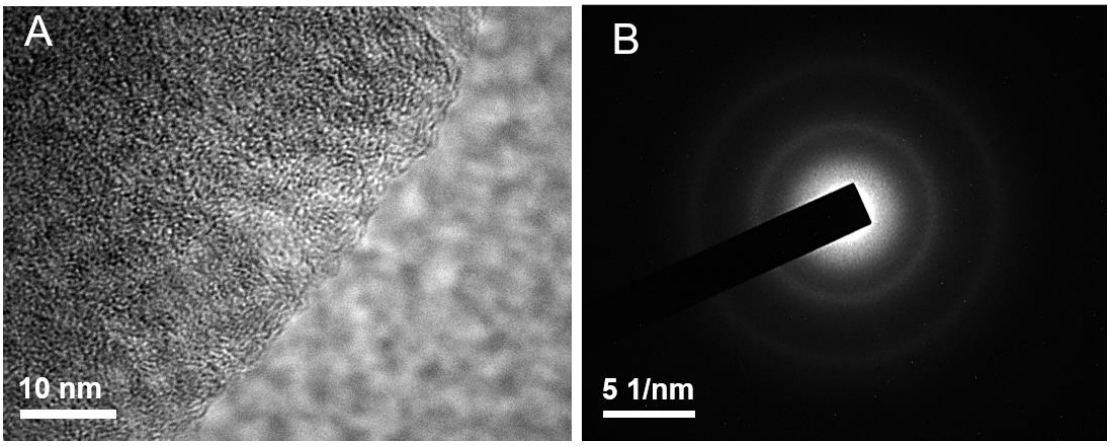

Fig. S4. **High-resolution TEM image and corresponding selected-area electron diffraction (SAED) pattern of the spiral MCNs.** (A) High-resolution TEM (HRTEM) image and (B) the corresponding SAED of the spiral MCNs prepared by the lamellar micelle spiral self-assembly strategy. It can be seen that the spiral MCNs possess an amorphous framework with rich defects.

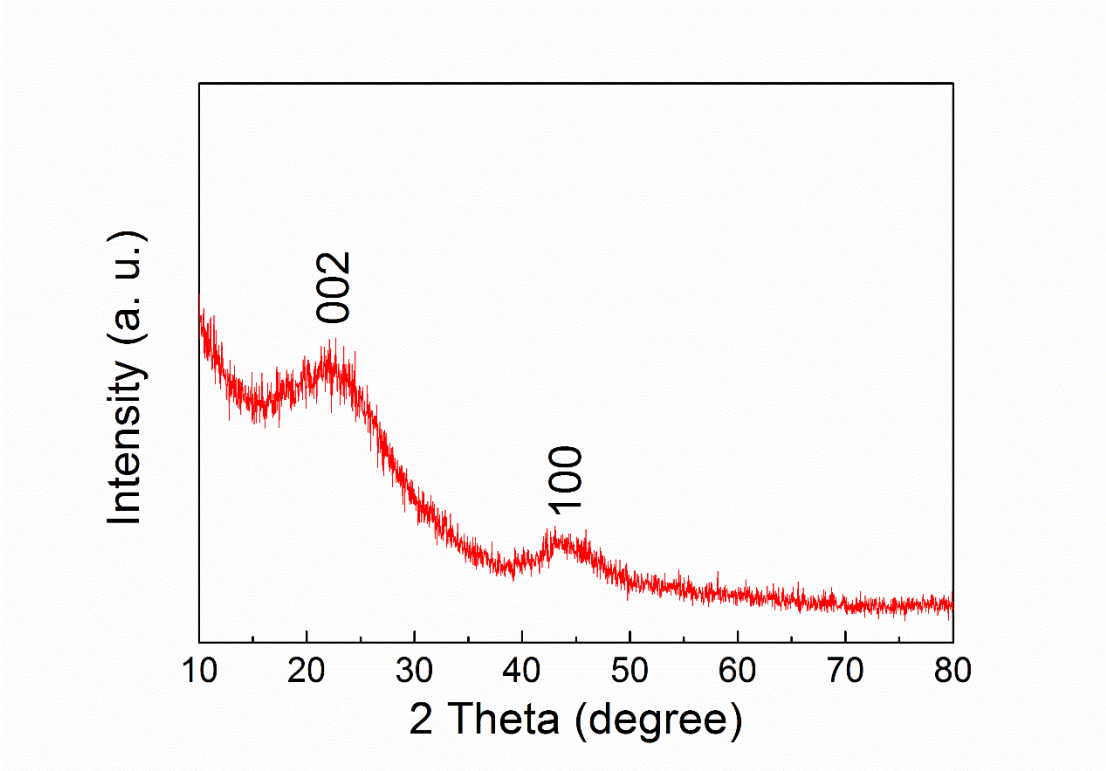

Fig. S5. **XRD pattern of the spiral MCNs**. The XRD pattern of the spiral MCNs prepared by the lamellar micelle spiral self-assembly strategy. The result shows two diffraction peaks near 22.6° and 44.0°, which can be indexed to the (002) and (100) planes of hard carbon, respectively. The averaged D_{002} interlayer distance is calculated to be 3.97 Å based on the Bragg's law, which is much larger than that of the natural graphite (3.35 Å), suggesting optimized amorphous feature.

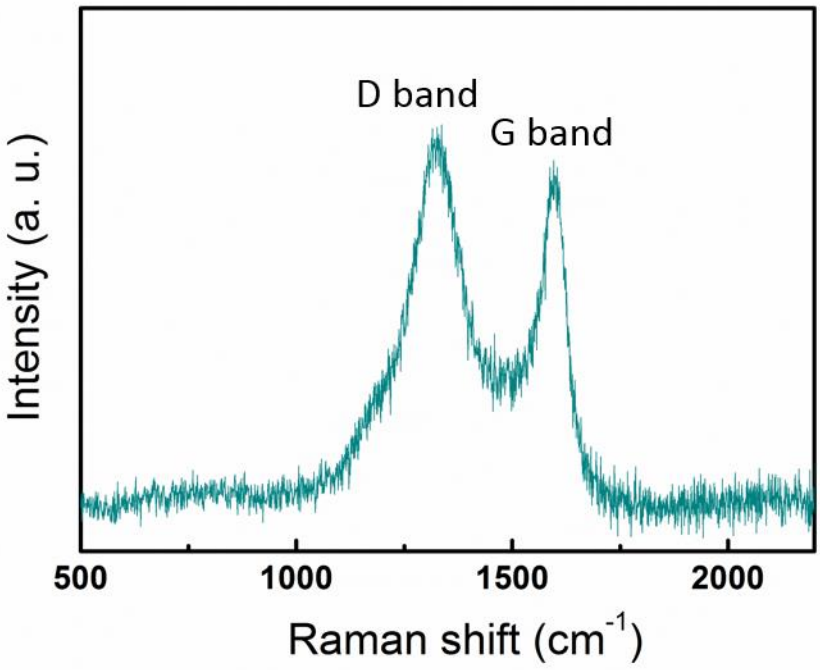

Fig. S6. Raman spectrum of the spiral MCNs. Raman spectrum of the spiral MCNs prepared by the lamellar micelle spiral self-assembly strategy. It can be seen that a high intensity ratio between the *D*-band (defect-induced band, 1346 cm^{-1}) and the *G*-band (crystalline graphite band, 1589 cm^{-1}), revealing a low graphitization degree of carbon framework.

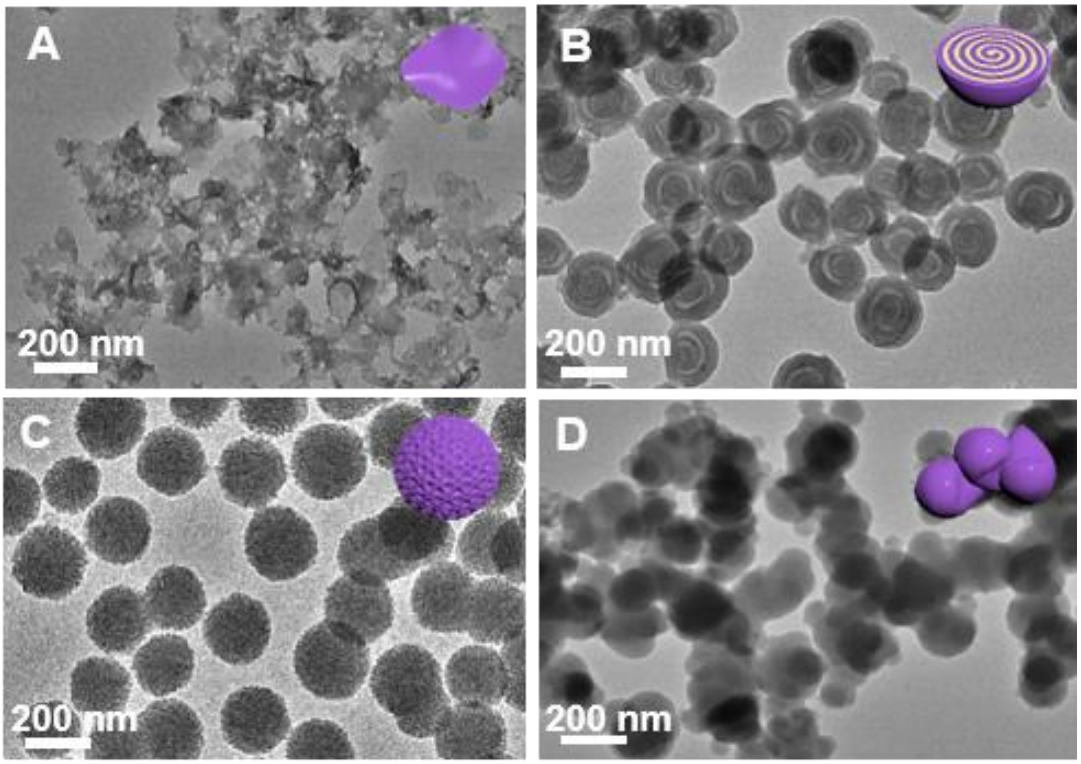

Fig. S7. The controlled experiments on the ethanol concentration. TEM images of the as-made PDA samples prepared by the lamellar micelle spiral self-assembly strategy using different volume fractions of ethanol: (A) 20 %, (B) 50 %, (C) 80 % and (D) 100 %. The results indicate that the as-made PDA samples can be tuned from irregular nanosheets, to multi-shelled nanospheres, to mesoporous nanospheres with worm-like pores, and to aggregated solid particles with the ethanol fractions changed from 20 to 100 %.

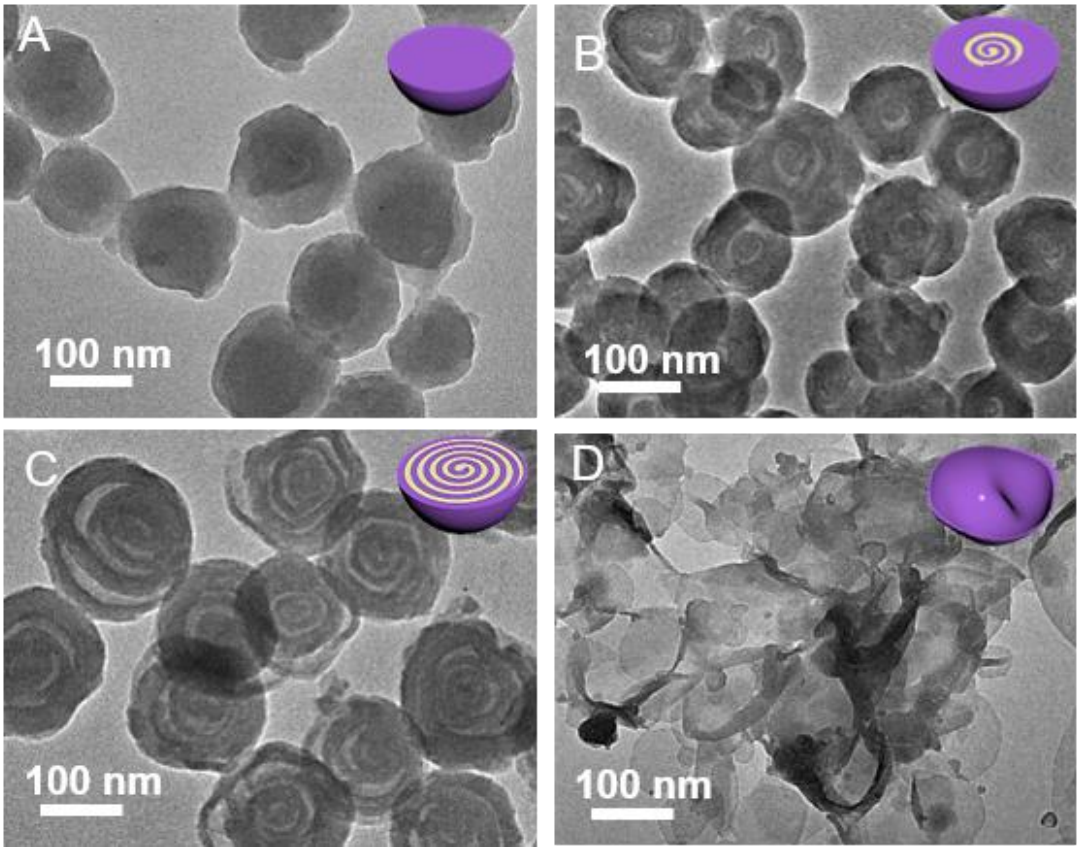

Fig. S8. **The controlled experiments on the TMB/P123 mass ratio**. TEM images of the as-made PDA samples prepared by the lamellar micelle spiral self-assembly strategy using different TMB/P123 mass ratios: (A) 0.2, (B) 0.4, (C) 0.8 and (D) 1.2. The results indicate that the structures of the products were varied from smooth solid nanospheres, to triple-shelled nanospheres, to quintuple-shelled nanospheres, and to stacked nanobowls with the TMB/P123 mass ratios changed from 0.2 to 1.2.

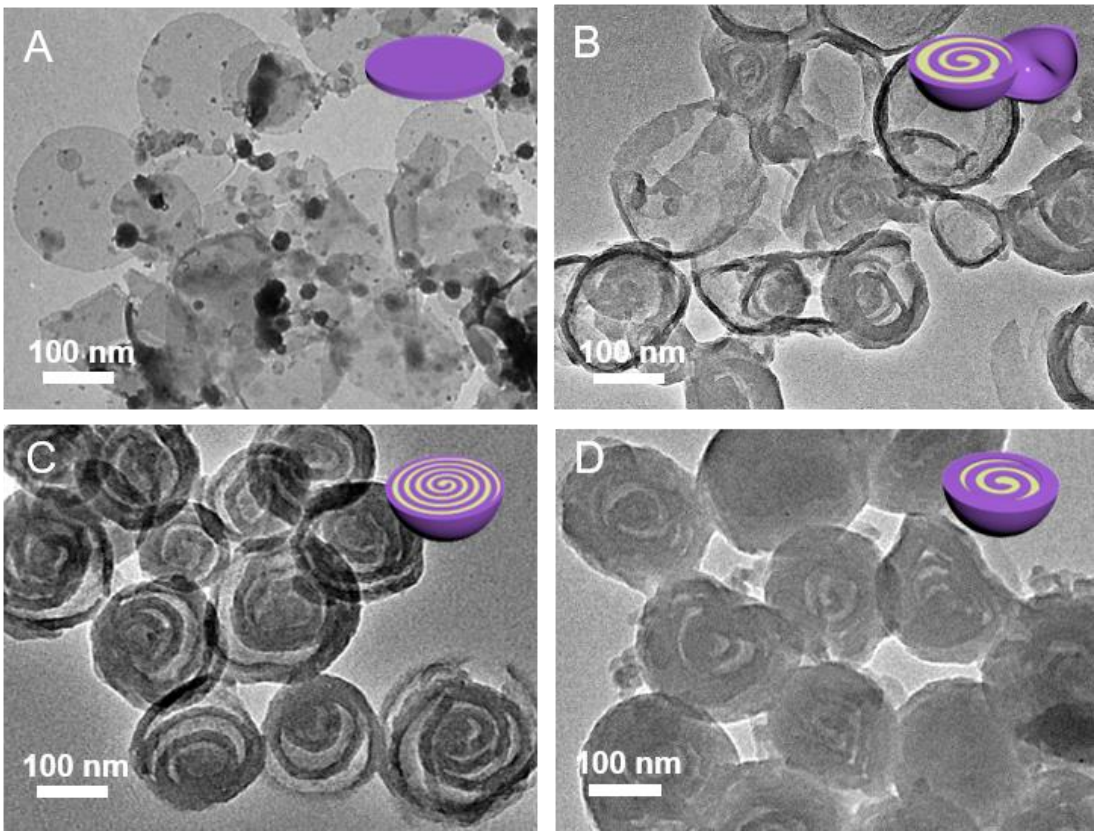

Fig. S9. The controlled experiments on the precursor amount. TEM images of the as-made PDA samples prepared by the lamellar micelle spiral self-assembly strategy using different dopamine amounts: (A) 0.25, (B) 0.50, (C) 0.75 and (D) 1.50 g. The results indicate that the structures of the products were varied from thin nanodisks, to a mixture of single hollow and defective multi-shelled nanospheres, to multi-shelled nanospheres, and to thick multi-shelled nanospheres with the dopamine amounts changed from 0.25 to 1.50 g.

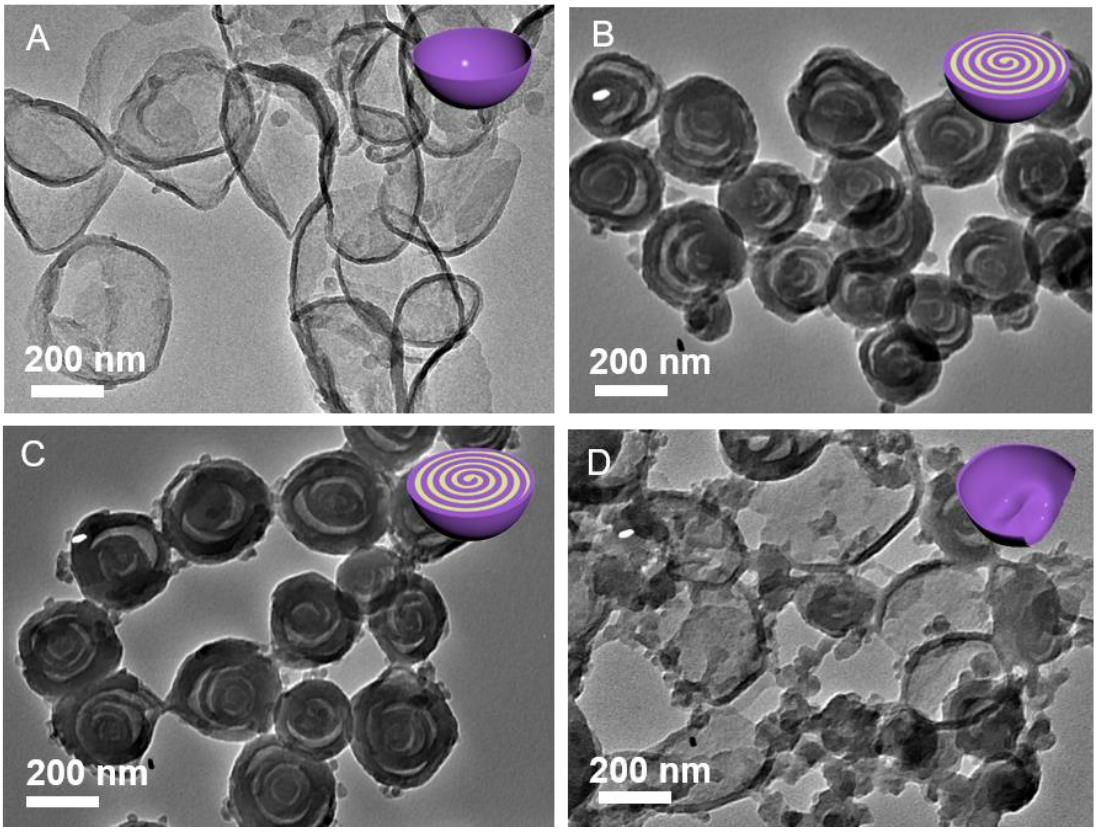

Fig. S10. The controlled experiments on the stirring rate. TEM images of the as-made PDA samples prepared by the lamellar micelle spiral self-assembly strategy under different stirring rates: (A) 0, (B) 300, (C) 700 and (D) 1000 rpm. The results indicate that insignificant change on the aspect of multi-shelled structure was demonstrated, while the stirring rate from 300 to 700 rpm were adopted. However, when a high stirring rate of 1000 rpm was used, the multi-shelled structure was destroyed, which is mainly attributed to the tearing force caused by the turbulence in the reaction system.

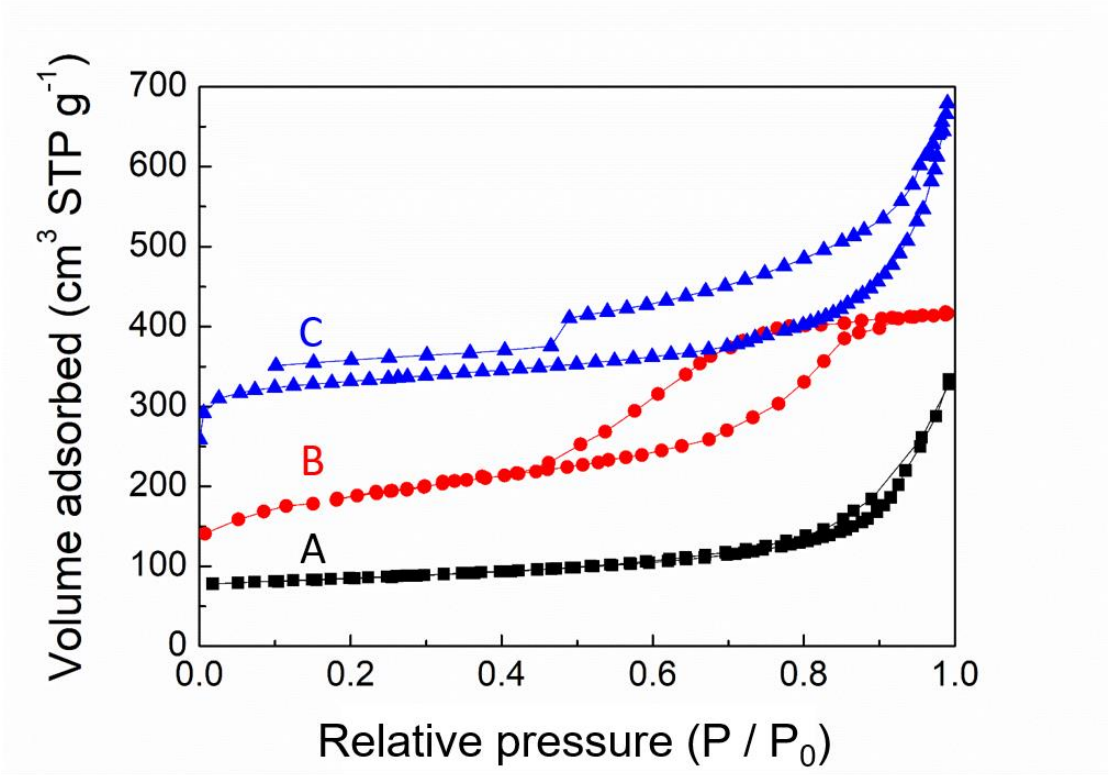

Fig. S11. **N_2 sorption isotherms of the mesoporous carbon nanospheres**. The N_2 sorption isotherms of the mesoporous carbon nanospheres prepared by the lamellar micelle spiral self-assembly strategy using different surfactants as templates: (A) F108, (B) F127 and (C) P105. The corresponding samples were denoted as MCN@F108, MCN@F127 and MCN@P105, respectively.

Tab. S1. Structure parameters of the mesoporous carbon nanospheres prepared by the lamellar micelle spiral self-assembly strategy using different surfactants as templates.

Sample	Surfactant	Molecular formula	M_r[a]	V_H/V_L[b]	BET surface area ($m^2\ g^{-1}$)	Pore volume ($cm^3\ g^{-1}$)	Pore size (nm)
MCN@F108	F108	$PEO_{132}PPO_{50}PEO_{132}$	14600	0.27	135	0.42	3
MCN@F127	F127	$PEO_{106}PPO_{70}PEO_{106}$	12600	0.46	413	0.73	7
MCN@P105	P105	$PEO_{37}PPO_{56}PEO_{37}$	6500	1.06	486	0.89	12
MCN@P123	P123	$PEO_{20}PPO_{70}PEO_{20}$	5800	2.43	530	1.00	16

M_r[a] was the average molecular weight of surfactants.

V_H/V_L[b] was the volume ratio between hydrophobic and hydrophilic blocks of surfactants.

The volume fraction (V_H/V_L) of the triblock copolymer was calculated as follow: Taking F127 (PEO_{106}-PPO_{70}-PEO_{106}) as an example：

$$\frac{V_H}{V_L} = \frac{M_{PPO}/\rho_{PPO}}{M_{PEO}/\rho_{PEO}} = \frac{4060/1.06}{9346/1.13} = \sim 0.46$$

In the equation, V_H and V_L represent the volumes of PPO and PEO blocks, respectively; M_{PPO} and M_{PEO} denote the molecular weights of the PPO and PEO blocks, respectively. ρ_{PPO} represents the density of PPO, which is about 1.13 g cm^{-3}, ρ_{PEO} expresses the density of PEO, which is about 1.06 g cm^{-3}. (*56*)

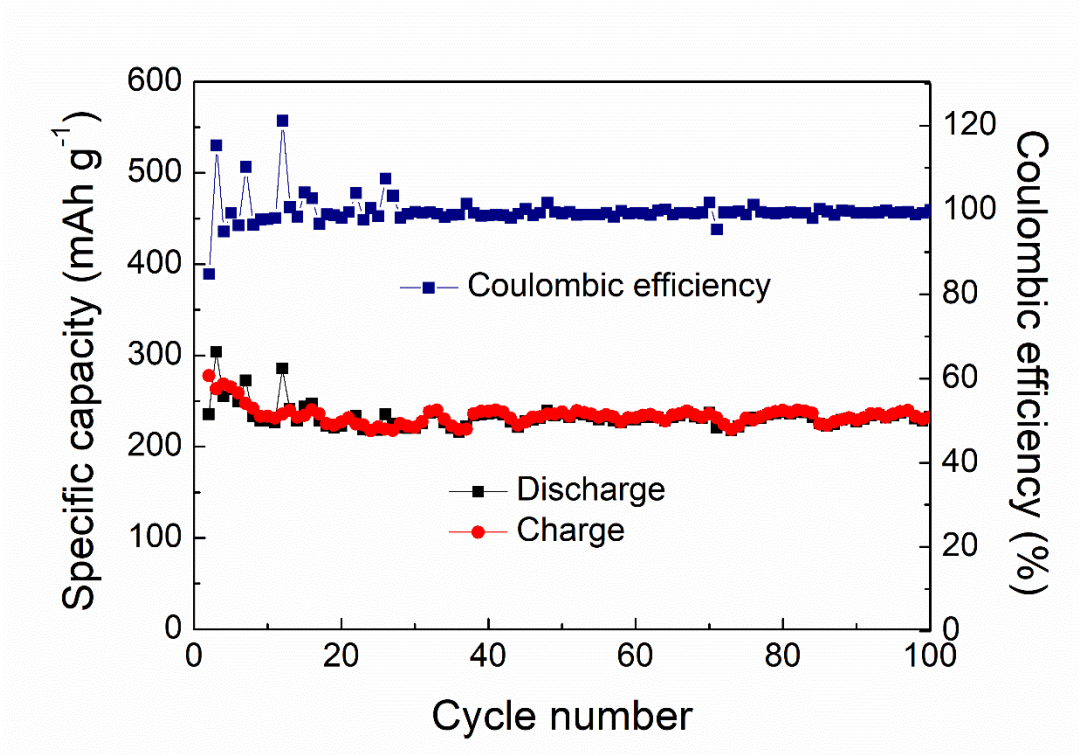

Fig. S12. **Reversible capacity tests of nonporous carbon particles (NCPs)**. The reversible capacity tests were carried out at a current density of 0.1 A g^{-1} for 100 cycles. The NCPs were synthesized by the lamellar micelle spiral self-assembly strategy except adding of TMB.

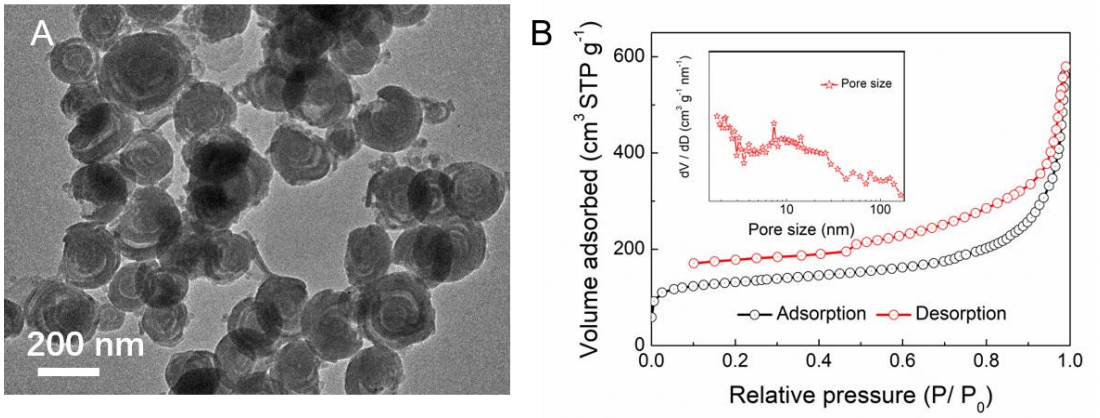

Fig. S13. **Characterizations of the spiral MCNs after cycling test.** TEM image (A) and N_2 sorption isotherms (B) of the spiral MCNs electrode after 40 charge/discharge cycles at a current density of 0.1 A g^{-1}. The inset of B is the corresponding pore size distribution. It can be seen that the spherical morphology and spiral multi-shelled structure can be well retained after a long-term cycle, which is consistent with its excellent electrochemical durability. Meanwhile, the N_2 sorption isotherms of the spiral MCNs show a type-IV curve and the corresponding pore size distribution is similar to the original curve before electrochemical test, further confirming that the structural advantages of the spiral MCNs.

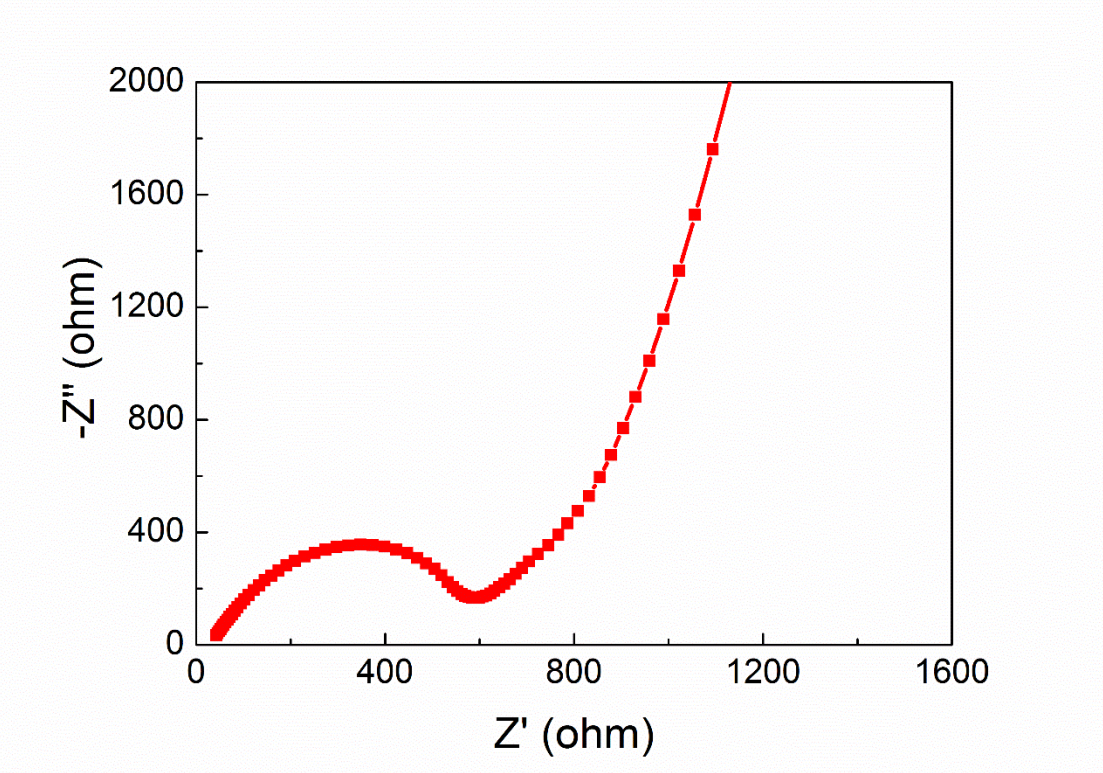

Fig. S14. Electrochemical impedance spectrum of the spiral MCNs electrode. The electrochemical impedance spectrum of the spiral MCNs electrode after 500th cycles at the current density of 2.0 A g^{-1}. The result shows a small semicircle diameter and high line slope in the moderate and low frequency regions, respectively, corresponding to a well-acknowledged character favorable for fast ions transportation.

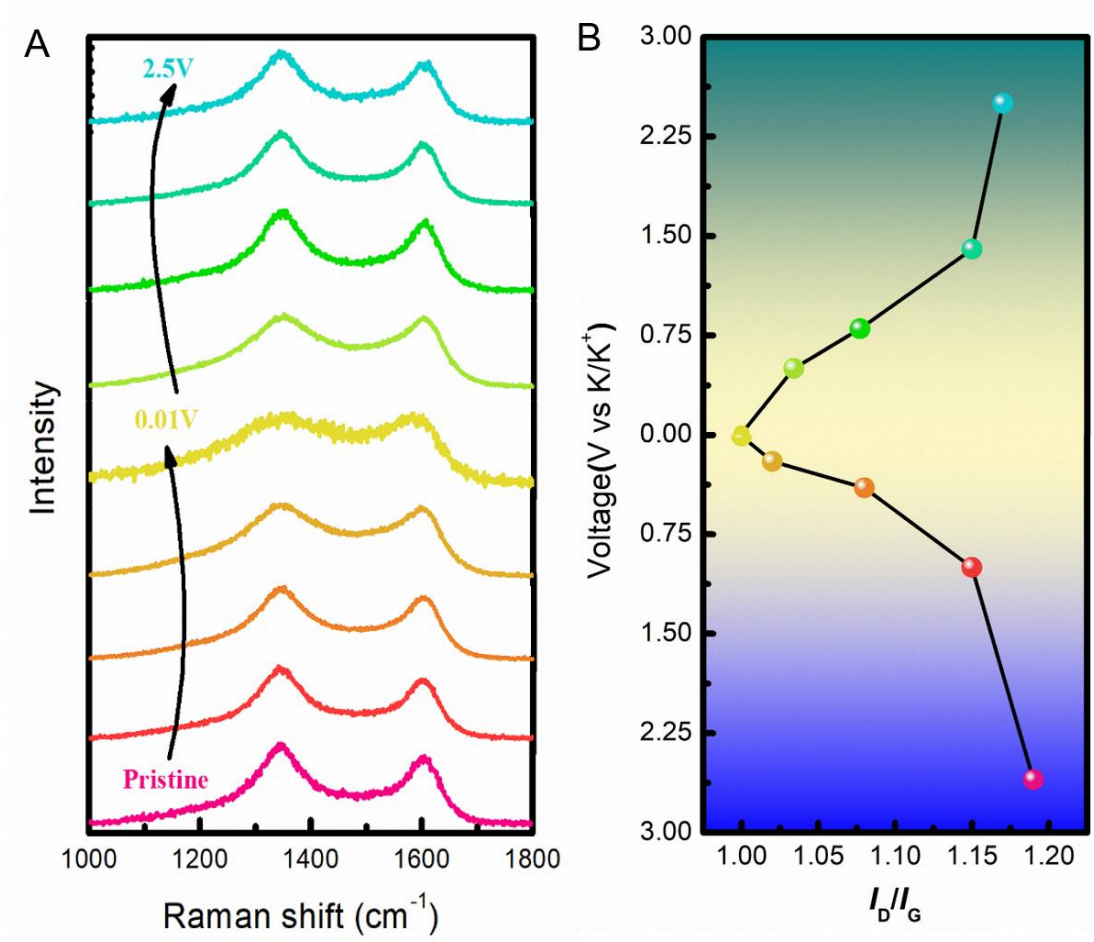

Fig. S15. *Ex-situ* Raman spectra of the spiral MCNs electrode. The *Ex-situ* Raman spectra (A) and the corresponding I_D/I_G ratios (B) of the spiral MCNs electrode for potassium ion battery. It can be seen that the I_D/I_G ratio continuously decreases from 1.18 to 1.01 during the potassiation process, indicating a decrease in the degree of amorphization. Then, the I_D/I_G ratios rises to 1.17 in the depotassiation process, which is close to the original value, suggesting that the charge/discharge process is nearly reversible.

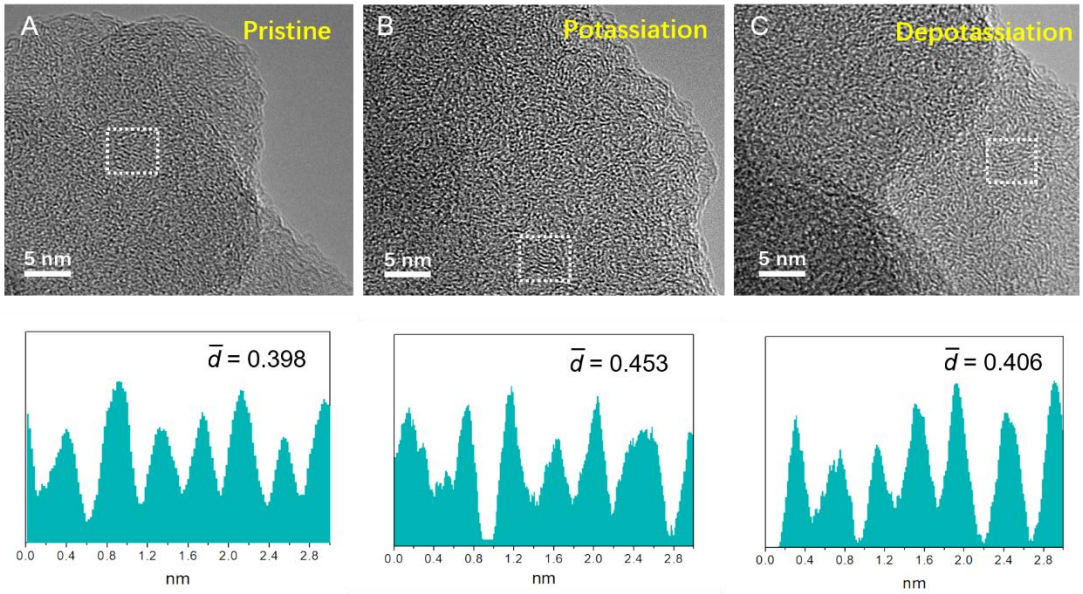

Fig. S16. *Ex-situ* HRTEM analysis of the spiral MCNs. The *Ex-situ* HRTEM analyses of the (A) pristine, (B) potassiation, and (C) depotassiation stages of the spiral MCNs in potassium ion battery. It can be seen that the pristine spiral MCNs has a short interlayer spacing of ~0.398 nm (A). The interlayer spacing then increased to ~0.453 nm after potassiaton (B), and finally switched back to ~0.406 nm after depotassiation (C). These results suggested that the structure of the amorphous carbon frameworks is nearly reversible during potassiaton/depotassiation process, thus enabling stable insertion/extraction of K-ion.

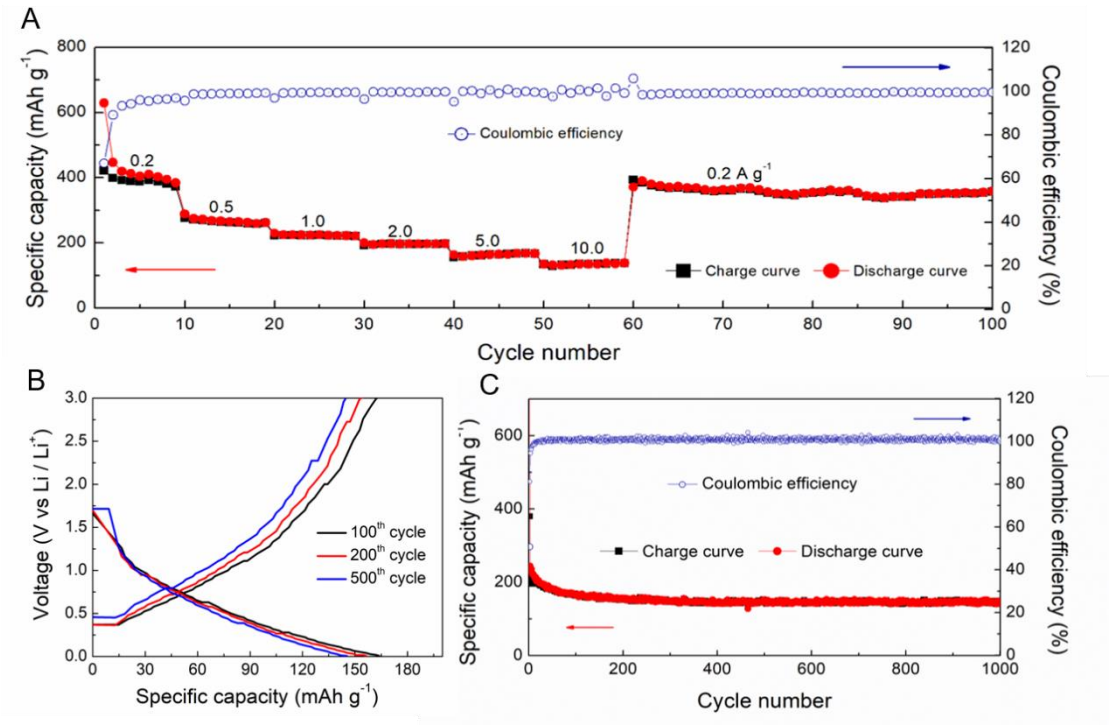

Fig. S17. Electrochemical performance of the spiral MCNs for lithium ion batteries. (A) Rate capability tests from 0.2 to 10.0 A g^{-1}, (B) charge/discharge curves and (C) cycling stability at 5.0 A g^{-1}.

The spiral MCNs were also tested as anode materials for LIBs in the CR2032-type coin half cells. The specific reversible capacities are calculated to be 394, 259, 223, 197 and 167 mAh g^{-1} at the current densities of 0.2, 0.5, 1.0, 2.0 and 5.0 A g^{-1}, respectively (Fig. S17A). Notably, a decent capacity of 128 mAh g^{-1} can be retained by further increasing the current density to 10.0 A g^{-1}. When the current rate was reset to 0.2 A g^{-1}, a reversible capacity of 375 mAh g^{-1} can be recovered, suggesting the excellent rate capability. After being tested at 5.0 A g^{-1} over 1000 cycles, the spiral MCNs electrode retained a stable capacity of 143 mAh g^{-1} with slight capacity decay of ~0.04 % per cycle (Fig S17B, C).

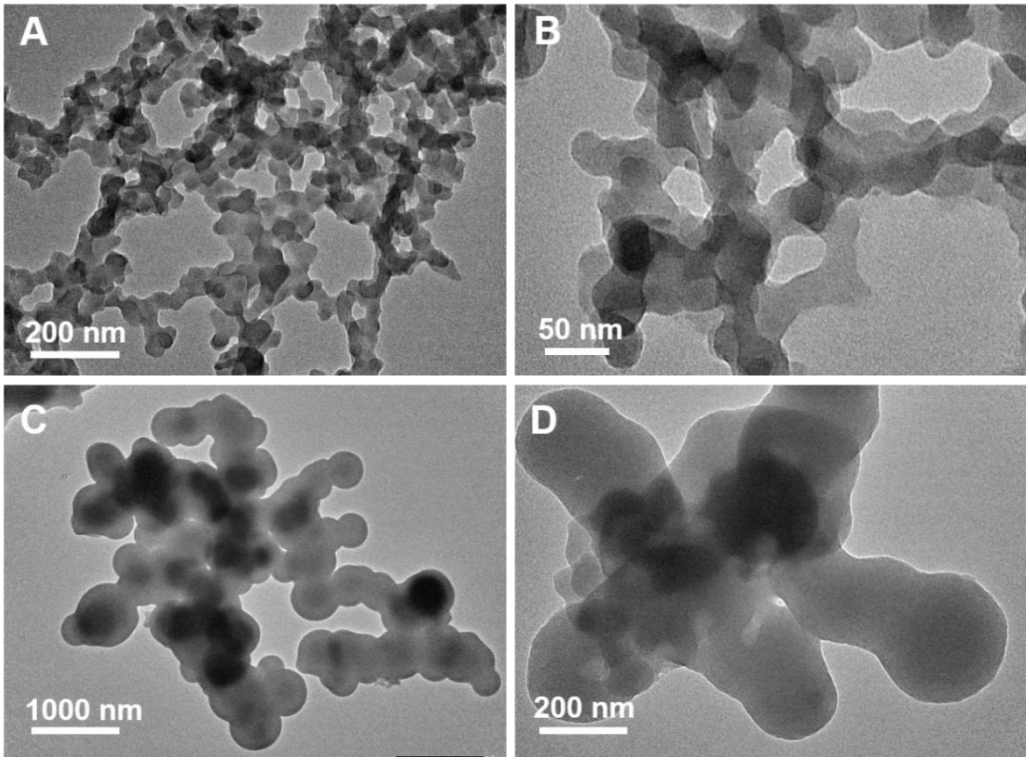

Fig. S18. TEM images of the nonporous PDA particles. The TEM images of the PDA particles prepared by the lamellar micelle spiral self-assembly strategy using PPO (A, B) or PEO (C, D) single-block copolymers as templates. It can be seen that only nonporous aggregated particles can be formed when absence of PEO or PPO blocks in surfactants.

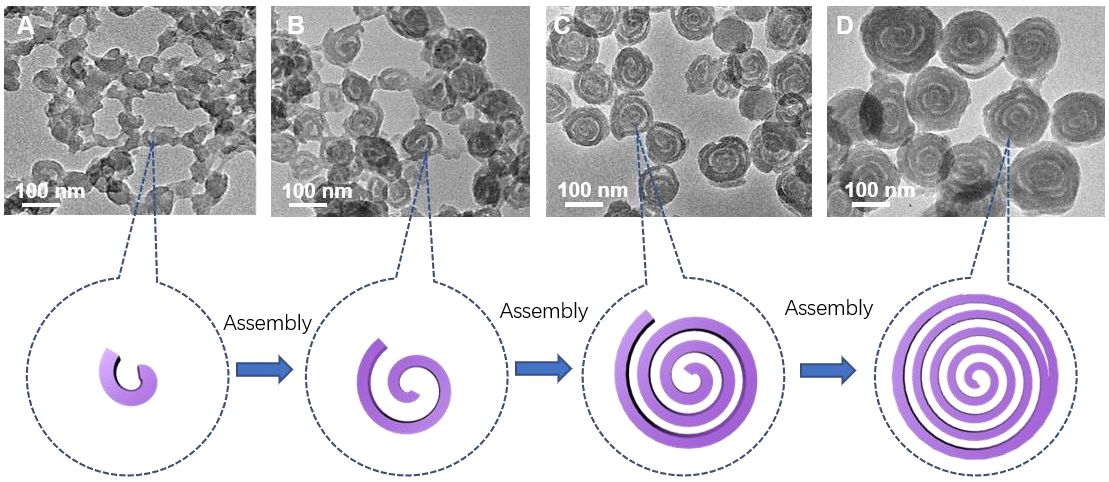

Fig. S19. **Structural evolution of multi-shelled nanosphere during self-assembly synthesis.** The TEM images and corresponding models of the as-made PDA nanospheres prepared at different reaction times: (A) 5 min, (B) 30 min, (C) 60 min, and (D) 180 min. Initially, the small nanoparticles with a spoon shape were formed (5 min, A). With the reaction going on, the spoon-like nanoparticles were gradually spiral self-assembled into the intermediated double-shelled (30 min, B) and quadruple-shelled PDA (60 min, D) nanospheres with open ends. Finally, the well-developed spiral multi-shelled PDA with clasp-ring at end were obtained (180 min, D).

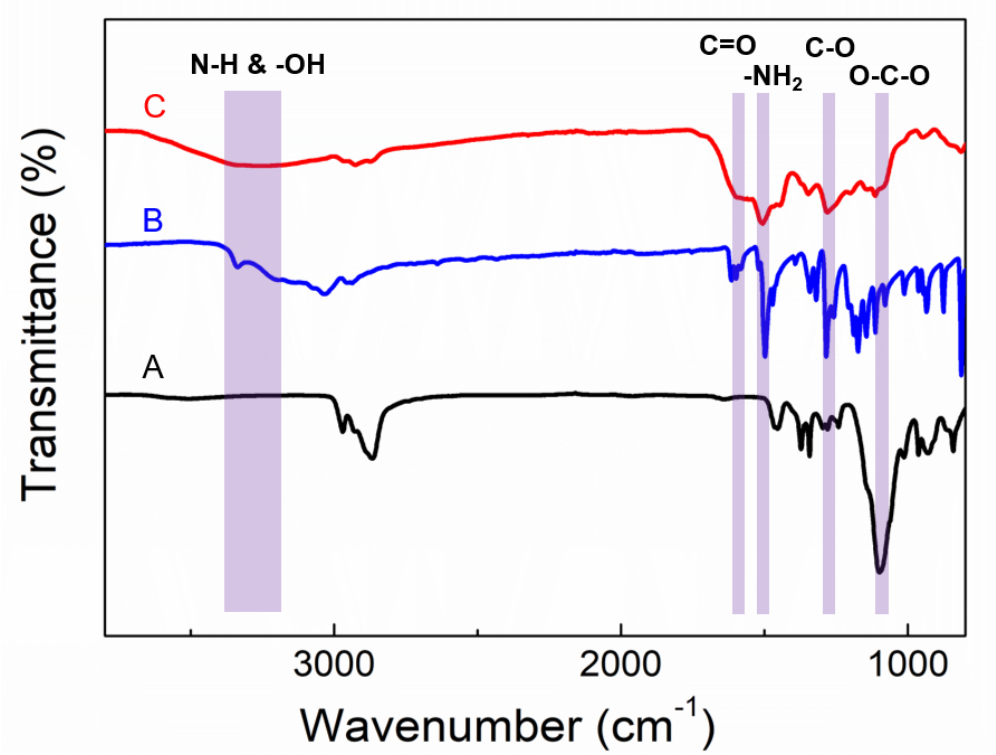

Fig. S20. FT-IR spectra of the as-made PDA nanospheres. The FT-IR spectrum of the Pluronic P123 (A), dopamine precursor (B) and (C) as-made PDA nanospheres. It can be seen that an absorption band at 3364 cm^{-1}, which ascribes to the stretching vibrations of –OH and N–H groups. The sharp peaks at 1612, 1495, 1280 and 1096 cm^{-1}, which corresponds to the C=O, $–NH_2$, C–O and C–O–C bonds, respectively. There results shown that the catechol and amino groups of dopamine can be oxidized to quinone and secondary amine groups, and meanwhile, DA and Pluronic P123 molecules appeared in the as-made PDA nanospheres.

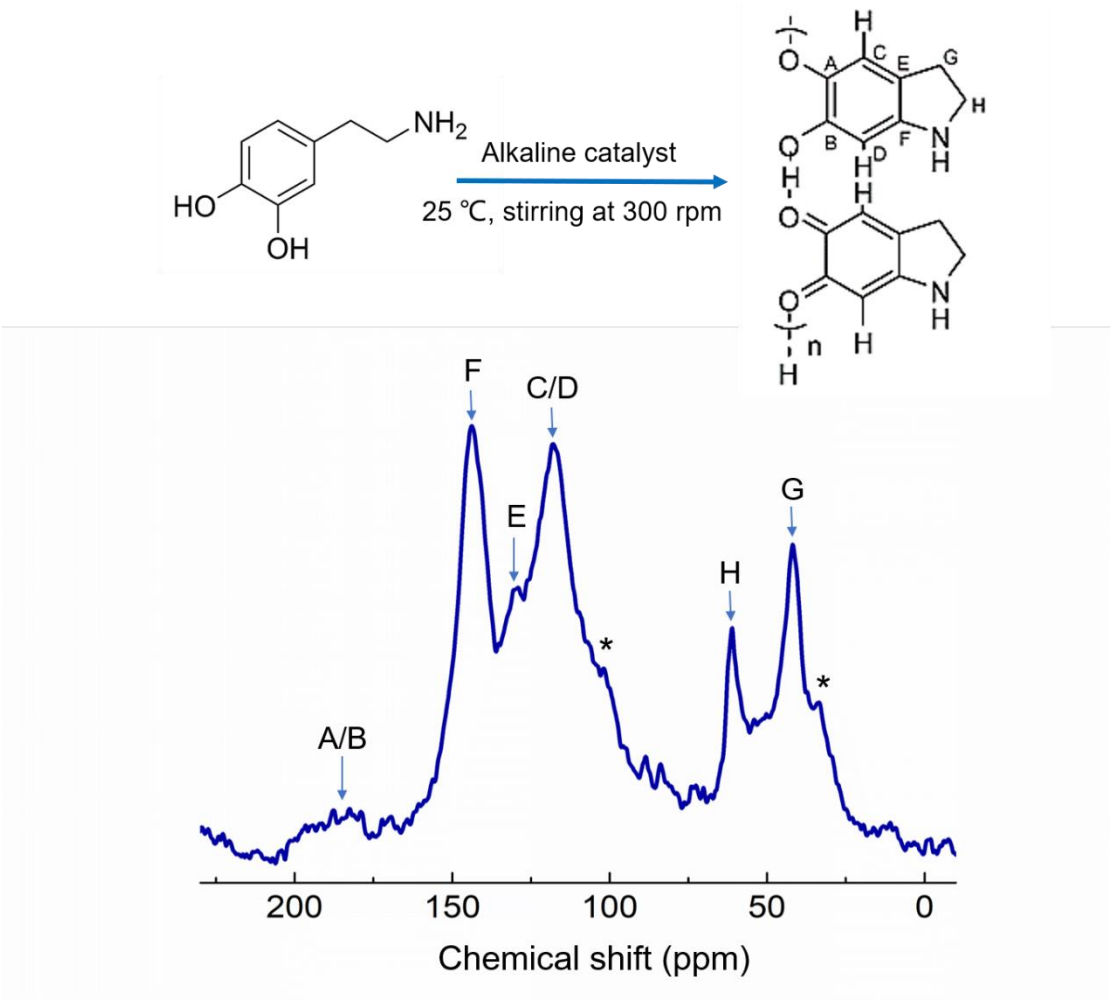

Fig. S21. **Solid state ^{13}C NMR spectrum of the as-made PDA nanospheres**. Before NMR test, the Pluronic P123 surfactant was removed by ethanol extraction. (*19*) It can be seen that a pair of resonances spanning from 100 to 150 ppm originated from the aromatic species (=CH–, =C–(OH)), suggesting that the aromatic ring of dopamine was retained. Meanwhile, a resonance observed at 173 ppm was assigned to 1,2-dione (O=C–) . In addition, the resonances observed from 30 to 70 ppm were corresponded to aliphatic species (–CH_2–N–, –CH_2–). (*57*) There results show that the PDA framework is primarily consisted of 5,6-dihydroxyindoline and 5,6-indoleindoline units.

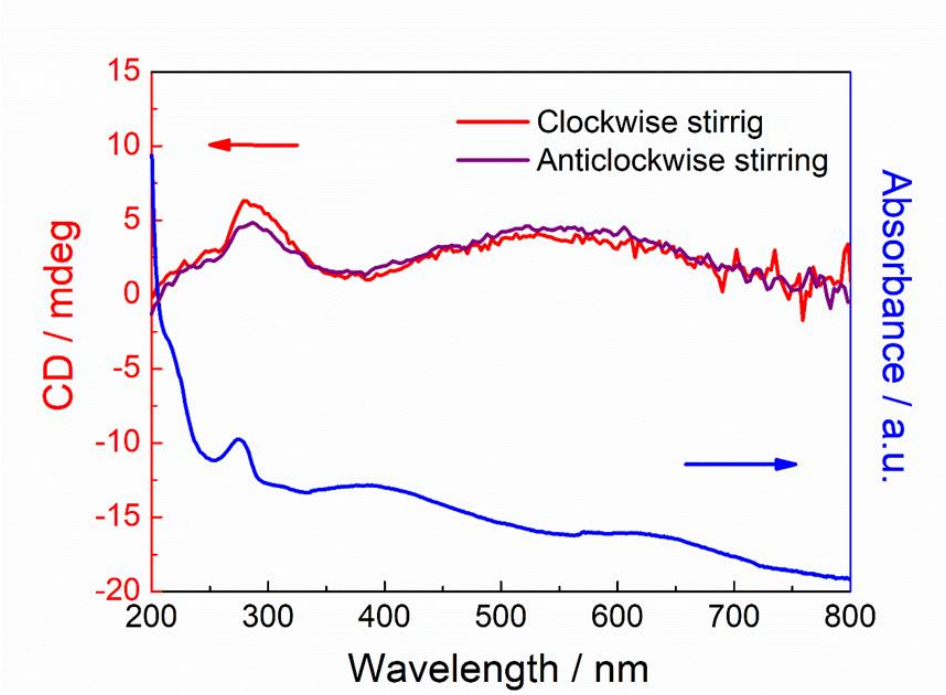

Fig. S22. CD and UV-vis spectra of the as-made PDA nanospheres. The spectra show one clear peak at ~280 nm, which ascribes to the typical adsorption of catechols in PDA, demonstrating the supramolecular chirality of the as-made polymer nanospheres (*58*). Meanwhile, a broad adsorption in a visible wavelength range (400-700 nm), which corresponds to the circularly polarized differential scattering from the spiral multi-shelled nanostructure (*59*). In addition, only positive signals can be obtained under both clockwise and anticlockwise stirrings, which indicates that the formed spiral multi-shelled nanostructure is independent of the stirring direction.

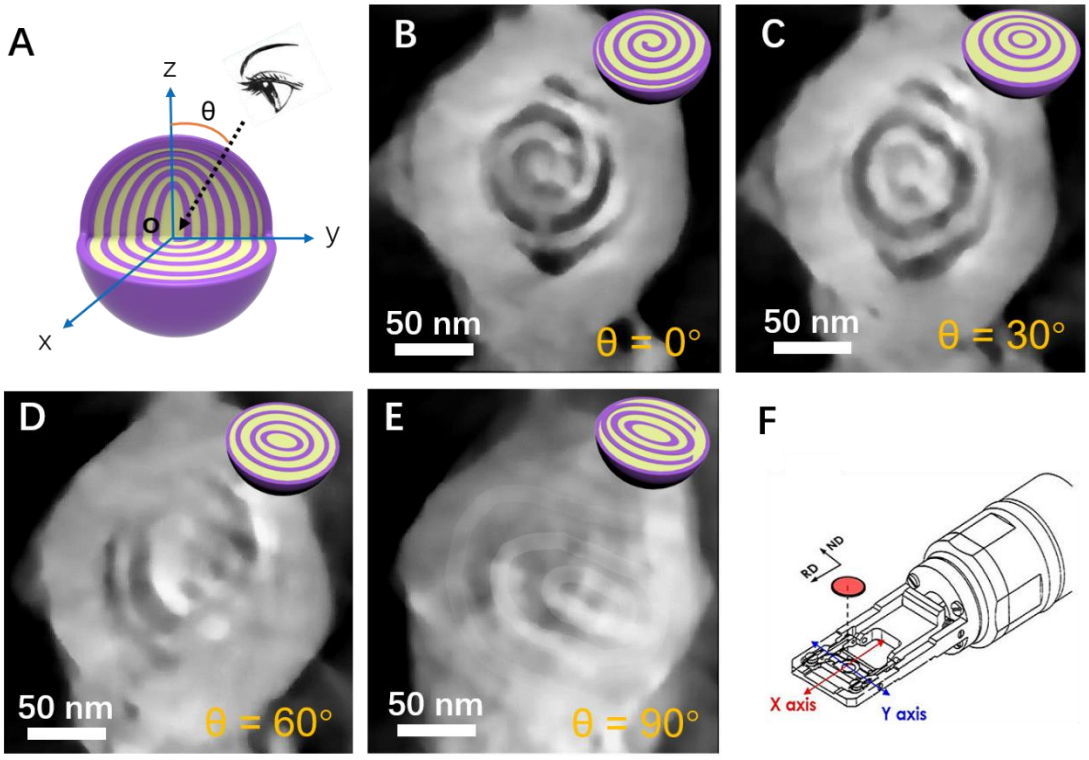

Fig. S23. Observation of the spiral multi-shelled nanostructure from multiple views. (A) Illustration of the viewing angle. (B-E) TEM images of the spiral MCNs at different viewing angles by rotating the holder around Y axis. (F) Illustration of the TEM specimen holder. As the holder rotated from 0° to 90°, the spherical morphology of the nanosphere retains, but the multi-shelled structure gradually changes from spiral, to onion-like, and to elliptic nanostructures, clearly indicating the uniquely spiral multi-shelled nanostructure.

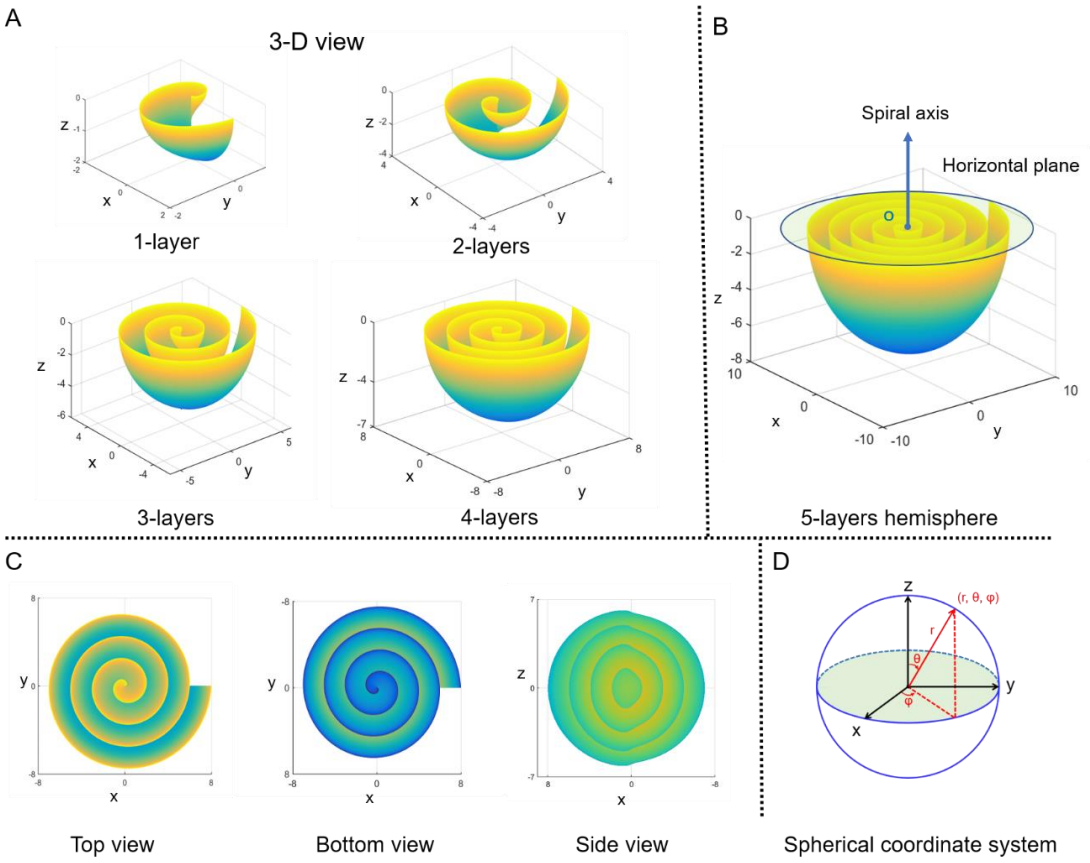

Fig. S24. Simulation of the spiral MCN at (A, B) 3-D, (C) top, bottom and side views. The geometric simulations were implemented in Matlab simulator based on the spherical coordinate system (D) and by using the following equation:

$$r = \frac{1}{\sqrt{(\frac{10\pi}{\varphi})^2 + (\cos\theta)^2}}$$

where r, φ, θ are the radial distance, polar angle and azimuth angle, respectively. According to this equation, the layer number of the multi-shelled model can be controlled from 1 to 5 layers by continuously altering the φ value from 2 π to 10 π (A, B), corresponding to the spiral self-assembly process shown in Fig S19. From the top and bottom views (C), anticlockwise and clockwise structures can be observed, which are consistent with the TEM results (Fig. 2E, F), confirming that the proposed spiral nanostructure is geometrically possible.

Movie S1. The TEM 3-D tomography of the spiral MCN. The movie is based on a series of 2-D TEM images of the spiral MCNs acquired with 1° tilt intervals.

Movie S2. The optical dynamic transformation process of the formation of spiral multi-shelled nanospheres. Real time. As the reaction goes on, the PDA nanoparticles gradually transform from spoon-like particle to multi-shelled nanospheres with spiral nanostructure. Meanwhile, the reaction solution experiences a series changes from a clear transparent solution to a light orange emulsion (1 min), then to a deep brown suspension (30 min), and finally to a black mixture (180 min).

Tab. S2. Comparison of the electrochemical performances of the spiral MCNs electrode in this work with some carbon-based electrodes reported in the literature.

Samples	Current density (mA g^{-1})	Initial capacity (mAh g^{-1})	Finial capacity (mAh g^{-1})	Cycle number	Capacity retention ratio (%)	References
Nitrogen/oxygen dual-doped hard carbon	50	320	230	100	71	(*60*)
Activated graphite nanosheet	200	318	126	100	40	(*61*)
Nitrogen-rich hard carbons	30	220	190	100	86	(*62*)
Nitrogen-doped graphene	100	270	210	100	78	(*63*)
Hierachically porous thin carbon shells	100	292	200	100	68	(*64*)
Short-range order in mesoporous carbon	50	310	256	100	82	(*65*)
Sulfur/oxygen codoped porous hard carbon microspheres	50	341	227	100	67	(*66*)
Hierarchical necklace-like N-doped hollow carbon	200	350	200	1000	57	(*67*)
Hollow carbon architecture	140	280	250	150	89	(*68*)
Highly nitrogen doped carbon nanofibers	25	350	248	100	71	(*69*)
Spiral multi-shelled carbon nanospheres (Spiral MCNs)	**100**	**371**	**291**	**100**	**79**	**This work**

REFERENCES AND NOTES

1. Y. Yang, X. Yang, L. Liang, Y. Gao, H. Cheng, X. Li, X. Zou, R. Ma, Q. Yuan, X. Duan, Large-area graphene-nanomesh/carbon-nanotube hybrid membranes for ionic and molecular nanofiltration. *Science* **364**, 1057–1062 (2019).

2. C. H. J. Evers, J. A. Luiken, P. G. Bolhuis, W. K. Kegel, Self-assembly of microcapsules via colloidal bond hybridization and anisotropy. *Nature* **534**, 364–368 (2016).

3. W. Li, J. Liu, D. Y. Zhao, Mesoporous materials for energy conversion and storage devices. *Nat. Rev. Mater.* **1**, 16023 (2016).

4. J. Liu, N. P. Wickramaratne, S. Z. Qiao, M. Jaroniec, Molecular-based design and emerging applications of nanoporous carbon spheres. *Nat. Mater.* **14**, 763–774 (2015)

5. J. Knossalla, D. Jalalpoor, F. Schüth, Hands-on guide to the synthesis of mesoporous hollow graphitic spheres and core-shell materials. *Chem. Mater.* **29**, 7062–7072 (2017).

6. J. Zhang, Z. Xia, L. Dai, Carbon-based electrocatalysts for advanced energy conversion and storage. *Sci. Adv.* **1**, e1500564 (2015)

7. N. P. Wickramaratne, J. Xu, M. Wang, L. Zhu, L. Dai, M. Jaroniec, Nitrogen enriched porous carbon spheres: Attractive materials for supercapacitor electrodes and CO_2 adsorption. *Chem. Mater.* **26**, 2820–2828 (2014).

8. H. Tian, J. Liang, J. Liu, Nanoengineering carbon spheres as nanoreactors for sustainable energy applications. *Adv. Mater.* **31**, 1903886 (2019).

9. H. Zhang, P. An, W. Zhou, B. Y. Guan, P. Zhang, J. Dong, X. W. D. Lou, Dynamic traction of lattice-confined platinum atoms into mesoporous carbon matrix for hydrogen evolution reaction. *Sci. Adv.* **4**, eaao6657 (2018).

10. F. Yuan, S. Li, Z. Fan, X. Meng, L. Fan, S. Yang, Shining carbon dots: Synthesis and biomedical and optoelectronic applications. *Nano Today* **11**, 565–586 (2016).

11. M. S. Kim, J. Lee, H. S. Kim, A. Cho, K. H. Shim, T. N. Le, S. S. A. An, J. W. Han, M. I. Kim, J. Lee, Heme cofactor-resembling Fe-N single site embedded graphene as nanozymes to selectively detect H_2O_2 with high sensitivity. *Adv. Funct. Mater.* **30**, 1905410 (2020).

12. W. Chen, G. Li, A. Pei, Y. Li, L. Liao, H. Wang, J. Wan, Z. Liang, G. Chen, H. Zhang, J. Wang, Y. Cui, A manganese-hydrogen battery with potential for grid-scale energy storage. *Nat. Energy* **3**, 428–435 (2018).

13. J. L. Xia, D. Yan, L. P. Guo, X. L. Dong, A. H. Lu, Hard carbon nanosheets with uniform ultramicropores and accessible functional groups showing high realistic capacity and superior rate performance for sodium-ion storage. *Adv. Mater.* **32**, 2000447 (2020).

14. T. Lin, I.-W. Chen, F. Liu, C. Yang, H. Bi, F. Xu, F. Huang, Nitrogen-doped mesoporous carbon of extraordinary capacitance for electrochemical energy storage. *Science* **350**, 1508–1513 (2015)

15. F. Han, R. Wang, B. Chen, Y. Feng, H. Liu, S. Wang, D. Su, H. Zhang, H. Chen, Precise dimerization of hollow fullerene compartments. *J. Am. Chem. Soc.* **142**, 15396–15402 (2020).

16. F. Han, R. Wang, Y. Feng, S. Wang, L. Liu, X. Li, Y. Han, H. Chen, On demand synthesis of hollow fullerene nanostructures. *Nat. Commun.* **10**, 1548 (2019).

17. J. Liang, Y. Jiao, M. Jaroniec, S. Z. Qiao, Sulfur and nitrogen dual-doped mesoporous graphene electrocatalyst for oxygen reduction with synergistically enhanced performance. *Angew. Chem. Int. Ed.* **51**, 11496–11500 (2012).

18. H. Peng, B. Yao, X. Wei, T. Liu, T. Kou, P. Xiao, Y. Zhang, Y. Li, Pore and heteroatom engineered carbon foams for supercapacitors. *Adv. Energy Mater.* **9**, 1803665 (2019)

19. L. Peng, C.-T. Hung, S. Wang, X. Zhang, X. Zhu, Z. Zhao, C. Wang, Y. Tang, W. Li, D. Zhao, Versatile nanoemulsion assembly approach to synthesize functional mesoporous carbon nanospheres with tunable pore sizes and architectures. *J. Am. Chem. Soc.* **141**, 7073–7080 (2019).

20. B. Y. Guan, S. L. Zhang, X. W. Lou, Realization of walnut-shaped particles with macro-/mesoporous open channels through pore architecture manipulation and their use in electrocatalytic oxygen reduction. *Angew. Chem. Int. Ed.* **57**, 6176–6180 (2018).

21. G. Zhan, H. C. Zeng, A synthetic protocol for preparation of binary multi-shelled hollow spheres and their enhanced oxidation application. *Chem. Mater.* **29**, 10104–10112 (2017).

22. F. Xie, L. Zhang, C. Ye, M. Jaroniec, S. Z. Qiao, The application of hollow structured anodes for sodium-ion batteries: From simple to complex systems. *Adv. Mater.* **31**, 1800492 (2019).

23. J. Tang, J. Liu, C. Li, Y. Li, M. O. Tade, S. Dai, Y. Yamauchi, Synthesis of nitrogen-doped mesoporous carbon spheres with extra-large pores through assembly of diblock copolymer micelles. *Angew. Chem. Int. Ed.* **54**, 588–593 (2015).

24. J. Tang, Y. Yamauchi, MOF morphologies in control. *Nat. Chem.* **8**, 638–639 (2016).

25. S. Kim, J. Hwang, J. Lee, J. Lee, Polymer blend directed anisotropic self-assembly toward mesoporous inorganic bowls and nanosheets. *Sci. Adv.* **6**, eabb3814 (2020)

26. S. Kim, M. Ju, J. Lee, J. Hwang, J. W. Lee, Polymer interfacial self-assembly guided two-dimensional engineering of hierarchically porous carbon nanosheets. *J. Am. Chem. Soc.* **142**, 9250–9257 (2020).

27. F. Pei, L. Lin, A. Fu, S. Mo, D. Ou, X. Fang, N. Zheng, A two-dimensional porous carbon-modified separator for high-energy-density Li-S batteries. *Joule* **2**, 323–336 (2018).

28. Z. Zhou, T. Liu, A. U. Khan, G. L. Liu, Block copolymer-based porous carbon fibers. *Sci. Adv.* **5**, eaau6852 (2019).

29. L. Peng, H. Peng, C.-T. Hung, D. Guo, L. Duan, B. Ma, L. Liu, W. Li, D. Zhao, Programmable synthesis of radially gradient-structured mesoporous carbon nanospheres with tunable core-shell architectures. *Chem* **7**, 1020–1032 (2021).

30. Q. Sun, B. He, X.-Q. Zhang, A.-H. Lu, Engineering of hollow core-shell interlinked carbon spheres for highly stable lithium-sulfur batteries. *ACS Nano* **9**, 8504–8513 (2015).

31. L. Wang, Q. Sun, X. Wang, T. Wen, J.-J. Yin, P. Wang, R. Bai, X.-Q. Zhang, L.-H. Zhang, A.-H. Lu, C. Chen, Using hollow carbon nanospheres as a light-induced free radical generator to overcome chemotherapy resistance. *J. Am. Chem. Soc.* **137**, 1947–1955 (2015).

32. Y. Cao, L. Xiao, M. L. Sushko, W. Wang, B. Schwenzer, J. Xiao, Z. Nie, L. V. Saraf, Z. Yang, J. Liu, Sodium ion insertion in hollow carbon nanowires for battery applications. *Nano Lett.* **12**, 3783–3787 (2012).

33. F. Pei, T. An, J. Zang, X. Zhao, X. Fang, M. Zheng, Q. Dong, N. Zheng, From Hollow carbon spheres to N-doped hollow porous carbon bowls: Rational design of hollow carbon host for Li-S batteries. *Adv. Energy Mater.* **6**, 1502539 (2016).

34. S. Yang, X. Feng, L. Zhi, Q. Cao, J. Maier, K. Müellen, Nanographene-constructed hollow carbon spheres and their favorable electroactivity with respect to lithium storage. *Adv. Mater.* **22**, 838–842 (2010).

35. H. Zhang, O. Noonan, X. Huang, Y. Yang, C. Xu, L. Zhou, C. Z. Yu, Surfactant-free assembly of mesoporous carbon hollow spheres with large tunable pore sizes. *ACS Nano* **10**, 4579–4586 (2016)

36. M. Li, Y. Zhang, X. Wang, W. Ahn, G. Jiang, K. Feng, G. Lui, Z. Chen, Gas pickering emulsion templated hollow carbon for high rate performance lithium sulfur batteries. *Adv. Funct. Mater.* **26**, 8408–8417 (2016).

37. D. Gu, H. Bongard, Y. Deng, D. Feng, Z. Wu, Y. Fang, J. Mao, B. Tu, F. Schüth, D. Zhao, An aqueous emulsion route to synthesize mesoporous carbon vesicles and their nanocomposites. *Adv. Mater.* **22**, 833–837 (2010).

38. C. Liu, X. Huang, J. Wang, H. Song, Y. Yang, Y. Liu, J. Li, L. Wang, C. Yu, Hollow mesoporous carbon nanocubes: Rigid-interface-induced outward contraction of metal-organic frameworks. *Adv. Funct. Mater.* **28**, 1705253 (2018).

39. T. Wang, Y. Sun, L. Zhang, K. Li, Y. Yi, S. Song, M. Li, Z. A. Qiao, S. Dai, Space-confined polymerization: Controlled fabrication of nitrogen-doped polymer and carbon microspheres with refined hierarchical architectures. *Adv. Mater.* **31**, 1807876 (2019).

40. C. Chen, H. Wang, C. Han, J. Deng, J. Wang, M. Li, M. Tang, H. Jin, Y. Wang, Asymmetric flasklike hollow carbonaceous nanoparticles fabricated by the synergistic interaction between soft template and biomass. *J. Am. Chem. Soc.* **139**, 2657–2663 (2017).

41. J. Liu, T. Yang, D. Wang, G. Q. Lu, D. Zhao, S. Z. Qiao, A facile soft-template synthesis of mesoporous polymeric and carbonaceous nanospheres. *Nat. Commun.* **4**, 2798 (2013)

42. D. S. Bin, Z. X. Chi, Y. Li, K. Zhang, X. Yang, Y. G. Sun, J. Y. Piao, A. M. Cao, L. J. Wan, Controlling the compositional chemistry in single nanoparticles for functional hollow carbon nanospheres. *J. Am. Chem. Soc.* **139**, 13492–13498 (2017).

43. M. Hu, A. A. Belik, M. Imura, Y. Yamauchi, Tailored design of multiple nanoarchitectures in metal-cyanide hybrid coordination polymers. *J. Am. Chem. Soc.* **135**, 384–391 (2013).

44. J. Wang, H. Tang, L. Zhang, H. Ren, R. Yu, Q. Jin, J. Qi, D. Mao, M. Yang, Y. Wang, P. Liu, Y. Zhang, Y. Wen, L. Gu, G. Ma, Z. Su, Z. Tang, H. Zhao, D. Wang, Multi-shelled metal oxides prepared via an anion-adsorption mechanism for lithium-ion batteries. *Nat. Energy* **1**, 16050 (2016).

45. J. Wang, J. Wan, D. Wang, Hollow multishelled structures for promising applications: Understanding the structure-performance correlation. *Acc. Chem. Res.* **52**, 2169–2178 (2019).

46. S. Liu, L. Han, Y. Duan, S. Asahina, O. Terasaki, Y. Cao, B. Liu, L. Ma, J. Zhang, S. Che, Synthesis of chiral TiO_2 nanofibre with electron transition-based optical activity. *Nat. Commun.* **3**, 1215 (2012).

47. W. Ma, F. Cheng, Y. Liu, Deep-learning-enabled on-demand design of chiral metamaterials. *ACS Nano* **12**, 6326–6334 (2018).

48. H. Yang, G. A. Ozin, C. T. Kresge, The role of defects in the formation of mesoporous silica fibers, films, and curved shapes. *Adv. Mater.* **10**, 883–887 (1998).

49. Y. Wu, G. Cheng, K. Katsov, S. W. Sides, J. Wang, J. Tang, G. H. Fredrickson, M. Moskovits, G. D. Stucky, Composite mesostructures by nano-confinement. *Nat. Mater.* **3**, 816–822 (2004).

50. S. Che, Z. Liu, T. Ohsuna, K. Sakamoto, O. Terasaki, T. Tatsumi, Synthesis and characterization of chiral mesoporous silica. *Nature* **429**, 281–284 (2004).

51. C. Tan, X. Qi, Z. Liu, F. Zhao, H. Li, X. Huang, L. Shi, B. Zheng, X. Zhang, L. Xie, Z. Tang, W. Huang, H. Zhang, Self-assembled chiral nanofibers from ultrathin low-dimensional nanomaterials. *J. Am. Chem. Soc.* **137**, 1565–1571 (2015).

52. K. Ariga, T. Mori, T. Kitao, T. Uemura, Supramolecular chiral nanoarchitectonics. *Adv. Mater.* **32**, 1905657 (2020).

53. K. S. Sing, Reporting physisorption data for gas/solid systems with special reference to the determination of surface area and porosity (Recommendations 1984). *Pure Appl. Chem.* **57**, 603–619 (1985).

54. E. Peled, S. Menkin, Review—SEI: Past, present and future. *J. Electrochem. Soc.* **164**, A1703–A1719 (2017).

55. W. J. Kim, S. M. Yang, Helical mesostructured tubules from Taylor vortex-assisted surfactant templates. *Adv. Mater.* **13**, 1191–1195 (2001).

56. Z. Lin, S. Liu, W. Mao, H. Tian, N. Wang, N. Zhang, F. Tian, L. Han, X. Feng, Y. Mai, Tunable self-assembly of diblock copolymers into colloidal particles with triply periodic minimal surfaces. *Angew. Chem. Int. Ed.* **129**, 7241–7246 (2017).

57. D. R. Dreyer, D. J. Miller, B. D. Freeman, D. R. Paul, C. W. Bielawski, Elucidating the structure of poly(dopamine). *Langmuir* **28**, 6428–6435 (2012).

58. F. Chen, Y. Xing, Z. Wang, X. Zheng, J. Zhang, K. Cai, Nanoscale polydopamine (PDA) meets π-π interactions: An interface-directed coassembly approach for mesoporous nanoparticles. *Langmuir* **32**, 12119–12128 (2016).

59. W. Jiang, Z.-b. Qu, P. Kumar, D. Vecchio, Y. Wang, Y. Ma, J. H. Bahng, K. Bernardino, W. R. Gomes, F. M. Colombari, A. Lozada-Blanco, M. Veksler, E. Marino, A. Simon, C. Murray, S. R. Muniz, A. F. De Moura, N. A. Kotov, Emergence of complexity in hierarchically organized chiral particles. *Science* **368**, 642–648 (2020).

60. J. Yang, Z. Ju, Y. Jiang, Z. Xing, B. Xi, J. Feng, S. Xiong, Enhanced capacity and rate capability of nitrogen/oxygen dual-doped hard carbon in capacitive potassium-ion storage. *Adv. Mater.* **30**, 1700104 (2018).

61. Z. Tai, Q. Zhang, Y. Liu, H. Liu, S. X. Dou, Activated carbon from the graphite with increased rate capability for the potassium ion battery. *Carbon* **123**, 54–61 (2017).

62. C. Chen, Z. Wang, B. Zhang, L. Miao, J. Cai, L. Peng, Y. Huang, J. Jiang, Y. Huang, L. Zhang, J. Xie, Nitrogen-rich hard carbon as a highly durable anode for high-power potassium-ion batteries. *Energ. Storage Mater.* **8**, 161–168 (2017).

63. K. Share, A. P. Cohn, R. Carter, B. Rogers, C. L. Pint, Role of nitrogen-doped graphene for improved high-capacity potassium ion battery anodes. *ACS Nano* **10**, 9738–9744 (2016).

64. A. Mahmood, S. Li, Z. Ali, H. Tabassum, B. Zhu, Z. Liang, W. Meng, W. Aftab, W. Guo, Y. Zhang, Ultrafast sodium/potassium-ion intercalation into hierarchically porous thin carbon shells. *Adv. Mater.* **31**, 1805430 (2019).

65. W. Wang, J. Zhou, Z. Wang, L. Zhao, P. Li, Y. Yang, C. Yang, H. Huang, S. J. Guo, Short-range order in mesoporous carbon boosts potassium-ion battery performance. *Adv. Energy Mater.* **8**, 1701648 (2018).

66. M. Chen, W. Wang, X. Liang, S. Gong, J. Liu, Q. Wang, S. Guo, H. Yang, Sulfur/oxygen codoped porous hard carbon microspheres for high-performance potassium-ion batteries. *Adv. Energy Mater.* **8**, 1800171 (2018).

67. W. Yang, J. Zhou, S. Wang, W. Zhang, Z. Wang, F. Lv, K. Wang, Q. Sun, S. Guo, Freestanding film made by necklace-like N-doped hollow carbon with hierarchical pores for high-performance potassium-ion storage. *Energ. Environ. Sci.* **12**, 1605–1612 (2019).

68. D.-S. Bin, X.-J. Lin, Y.-G. Sun, Y.-S. Xu, K. Zhang, A.-M. Cao, L.-J. Wan, Engineering hollow carbon architecture for high-performance K-ion battery anode. *J. Am. Chem. Soc.* **140**, 7127–7134 (2018).

69. Y. Xu, C. Zhang, M. Zhou, Q. Fu, C. Zhao, M. Wu, Y. Lei, Highly nitrogen doped carbon nanofibers with superior rate capability and cyclability for potassium ion batteries. *Nat. Commun.* **9**, 1720 (2018).